FULL PAPER

Interdispersed Amorphous MnOx–Carbon Nanocomposites with Superior Electrochemical Performance as Lithium-Storage Material

*Juchen Guo, Qing Liu, Chunsheng Wang,* and Michael R. Zachariah**

The realization of manganese oxide anode materials for lithium-ion batteries is hindered by inferior cycle stability, rate capability, and high overpotential induced by the agglomeration of manganese metal grains, low conductivity of manganese oxide, and the high stress/strain in the crystalline manganese oxide structure during the repeated lithiation/delithiation process. To overcome these challenges, unique amorphous MnOx–C nanocomposite particles with interdispersed carbon are synthesized using aerosol spray pyrolysis. The carbon filled in the pores of amorphous MnOx blocks the penetration of liquid electrolyte to the inside of MnOx, thus reducing the formation of a solid electrolyte interphase and lowering the irreversible capacity. The high electronic and lithium-ion conductivity of carbon also enhances the rate capability. Moreover, the interdispersed carbon functions as a barrier structure to prevent manganese grain agglomeration. The amorphous structure of MnOx brings additional benefits by reducing the stress/strain of the conversion reaction, thus lowering lithiation/delithiation overpotential. As the result, the amorphous MnOx-C particles demonstrated the best performance as an anode material for lithium-ion batteries to date.

1. Introduction

Lithium-ion batteries are currently being used to power portable electronic devices such as laptop computers, cell phones, and digital cameras. They also are a very promising energy storage technology to meet the demands from some fast emerging applications including plug-in electric vehicles and integrated grid systems. To improve the current Li-ion battery technology, it is essential to use high-capacity materials such as silicon, tin, and transition metal oxides to replace the current carbon-based anodes.[1]

Transition metal oxides as anode materials were first proposed by Poizot et al. in 2000.[2] Among all the metal oxides

that can be used as anode for Li-ion batteries, manganese oxides was proven to be a superior choice due to its relatively lower electromotive force, i.e., lower thermodynamic equilibrium voltage versus Li/Li+,[3] its natural abundance, and its environmental benignity. The Li-storage mechanism of manganese oxides is based on the reversible oxidation/reduction reaction between Li and manganese oxides as shown in the following reaction, assuming complete conversion of the metal oxides.

$$MnO_x + 2xLi \leftrightarrow Mn + xLi_2O$$
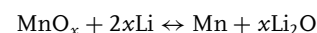
This reversible conversion mechanism is enabled by the formation of nanometer-sized (<5 nm) Mn grains uniformly dispersed in a Li2O matrix during the manganese oxide reduction reaction (forward reaction).[4–6] The nanometer-sized Mn grains create a large contact surface between metal and Li2O that makes the reverse reaction kinetically favorable. A variety of manganese oxide (MnO,[7–12] Mn2O3,[11,12] MnO2,[12–17] and Mn3O4[12,18–20]) anode materials have been investigated. The reversibility of conversion reaction depends on the MnOx phase structure, oxygen content x in MnOx and particle size. However, the realization of manganese oxide anodes is still hindered by several challenges including: 1) poor cycling stability due to structural instability caused by gradual agglomeration of the metal grains, and the large volume change during phase transformation in the conversion reaction;[21,22] 2) inferior rate capability, i.e., capability to be charged and discharged rapidly while maintaining high capacity, due to low electronic conductivity of manganese oxides; 3) low coulombic efficiency; and 4) high potential hysteresis between lithiation and delithiation due to high accommodation energy associated with a large volume change.

Current techniques to overcome these challenges were to reduce the particle size of manganese oxides to the nanometer scale to accommodate the large volume change. Carbon nanomaterials were also incorporated to enhance the electronic conductivity.[8–11,13–24] Graphene,[20] carbon nanotubes,[17,23] and carbon nanofibers[24] hae been used to fabricate manganese oxide–carbon nanocomposite anode materials. However, the high surface area of manganese oxide–carbon nanocomposites resulted in low coulombic efficiency due to the formation of a large unstable solid electrolyte interphase (SEI) during

Dr. J. Guo, Prof. C. Wang
Department of Chemical and Biomolecular Engineering
University of Maryland
College Park, MD 20742, USA
E-mail: cswang@umd.edu
Q. Liu, Prof. M. R. Zachariah
Department of Chemistry and Biochemistry
University of Maryland
College Park, MD 20742, USA
E-mail: mrz@umd.edu

**ADVANCED
FUNCTIONAL
MATERIALS**

www.afm-journal.de

*Materials
Views*

www.MaterialsViews.com
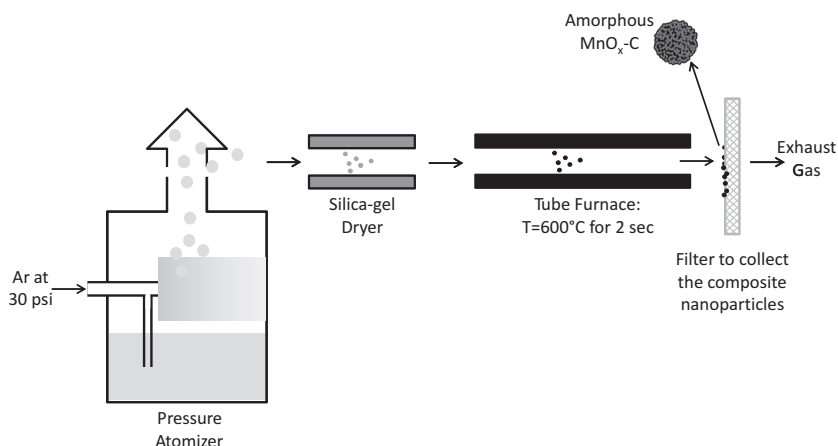
Figure 1. Diagram of the aerosol spray pyrolysis apparatus.

lithiation/delithiation cycles. The agglomeration of manganese grains and phase transformation of crystalline manganese oxides during cycling also limited the cycling stability.[7,8] Moreover, the large volume change during phase transformation of crystalline manganese oxides decreased the conversion reaction rate, resulting in a low lithiation potential. It was reported that crystalline MnO particle composed of nanometer-sized (10–30 nm) MnO grains could be lithiated at a potential that was 0.4 V higher than the bulk MnO particle due to the enhanced conversion reaction kinetics.[8] Maier and co-workers also reported that amorphization of crystalline RuO_2 could enhance the lithiation potential owing to the enhanced Gibbs free energy compared with the crystalline bulk RuO_2.[25] These studies suggest that amorphous manganese oxide may be able to narrow the potential hysteresis and achieve faster conversion reaction rates.

Therefore, an ideal structure might comprise a porous amorphous manganese oxide particle filled with carbon in the pores. The interdispersed carbon would facilitate the transport of Li^+ ions and electrons without increasing the undesirable surface area between electrolyte and active materials. Another import function of the carbon is to prevent the agglomeration of the Mn grains during cycling as a barrier structure.

In this study, carbon-filled manganese oxide–carbon nanocomposite particles were synthesized using aerosol spray pyrolysis, as illustrated in **Figure 1**. The resulting nanoparticles had a unique structure of uniformly inter-dispersed amorphous manganese oxide (MnO_x) and carbon. These MnO_x–C composite nanoparticles demonstrated high Li-storage capacity and superior cycling stability. Moreover, they also demonstrated impressive rate capacity and low charge/discharge voltage hysteresis. These amorphous MnO_x–C

nanoparticles have demonstrated the best electrochemical performance of manganese oxide anode to date.

2. Results and Discussion

2.1. Nanostructure Characterization

The transmission electron microscopy (TEM) image and the element mapping of the MnO_x–C composite nanoparticles are shown in **Figure 2**. The element mapping images in Figure 2b clearly demonstrated that the MnO_x–C nanoparticle had a homogeneous structure with uniform interdispersion of MnO_x and carbon. The TEM image and the selected-area electron diffraction (SAED) pattern shown in Figure 2a indicated the amorphous nature of the MnO_x–C nanoparticles, which was verified on the bulk sample from X-ray diffraction (XRD), shown in **Figure 3**. On the other hand, the XRD pattern of the pure manganese oxide nanoparticle, synthesized using the same pyrolysis procedure but without sucrose, demonstrated a majority Mn_3O_4 (70 mol%) crystalline phase, with a small fraction of crystalline Mn_2O_3 (30 mol%). The pure
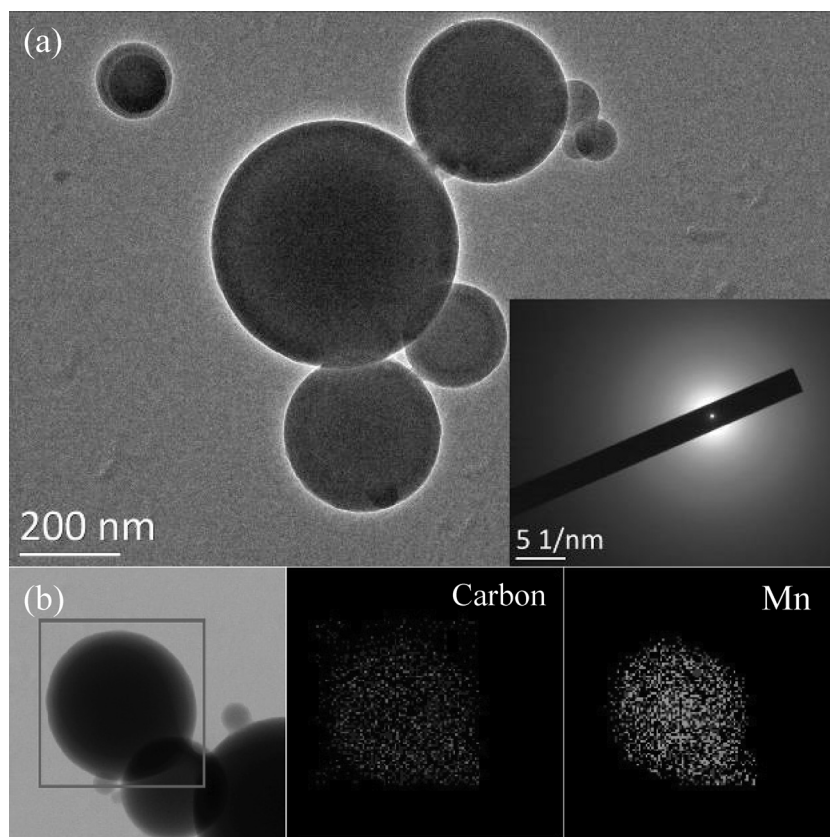
Figure 2. a) TEM and SAED images of the amorphous MnO_x–C nanoparticles; b) energy-dispersive X-ray spectroscopy (EDS) mapping image of distribution of elemental carbon and Mn in the amorphous MnO_x–C nanoparticles.

www.MaterialsViews.com

ADVANCED
FUNCTIONAL
MATERIALS
www.afm-journal.de

FULL PAPER
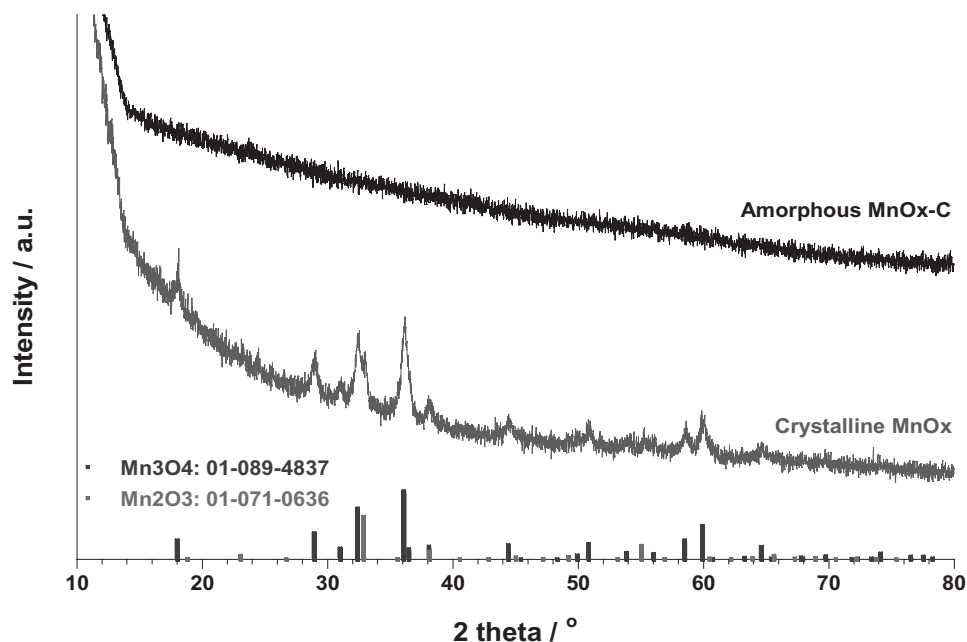
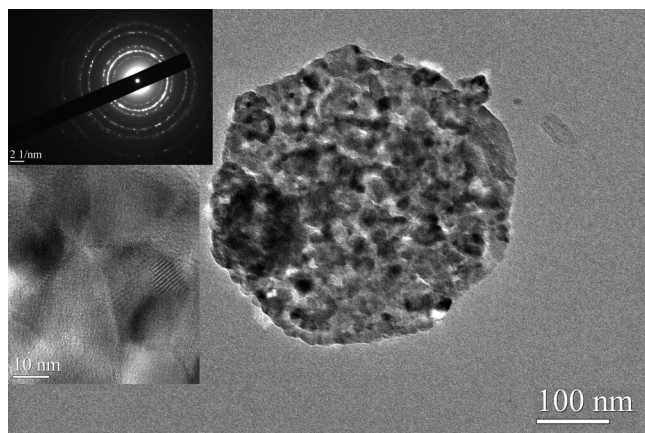**Figure 3.** XRD patterns of the amorphous MnO$_x$–C nanoparticles and the crystalline MnO$_x$ nanoparticles.

manganese oxide nanoparticle clearly shows a porous structure, as shown in **Figure 4,** consisting of a compact aggregate of much smaller crystalline particles. Apparently the addition of sucrose played a critical role in the formation of the homogeneous amorphous MnO$_x$–C nanoparticles, and suppression of crystallization of manganese oxide. It is likely that the nitrate decomposes first, but has insufficient time to create larger MnO$_x$ clusters, before the pyrolysis of sucrose leads to a carbon network blocking grain growth.

The oxidation state x in the amorphous MnO$_x$ was determined using X-ray photoelectron spectroscopy (XPS). Since the mixed oxidation state of Mn is not easily determined using standard manganese oxide compounds as references, the crystalline MnO$_x$ particles prepared in this study were used as the reference. Figure S1 in Supporting Information

Figure 4. TEM, SAED, and high-magnification TEM images of the crystalline MnO$_x$ nanoparticles.

shows the Mn 2p spectra of the amorphous MnO$_x$–C and the crystalline MnO$_x$. The two peaks located at 640.8 eV and 652.7 eV that can be attributed to Mn 2p3/2 and Mn 2p1/2, respectively, are identical in the two samples. Therefore, we conclude that the oxidation state of the amorphous MnO$_x$–C composite is the same as that of the crystalline pure MnO$_x$ and thus the nitrate decomposition and oxidation state is unaffected by the carbon reducing environment. From the XRD data, we determine the crystalline MnO$_x$ consisted of 70 mol% Mn$_3$O$_4$ and 30 mol% Mn$_2$O$_3$. Therefore, the oxidation state of amorphous MnO$_x$–C can be estimated as $x =$ 1.37. From the oxidation state of the manganese, the theoretical capacity of both amorphous MnO$_x$ and crystalline MnO$_x$ can be calculated as 961 mAh g^{-1} based on assuming complete reaction between MnO$_x$ and Li.

The carbon content in the amorphous MnO$_x$–C particles was determined by thermogravimetric analysis (TGA) oxidation with air. As shown in Figure S2 in the Supporting Information, complete carbon loss (oxidation) occurs by ~300 °C. The final weight retention at 500 °C was 38.4 wt.%. Assuming manganese oxide only exists in the most stable form, Mn$_3$O$_4$, at 500 °C, we can based on the final weight retention of 38.4%, determine the carbon and MnO$_x$ content in the MnO$_x$–C nanoparticles as 61 wt.% and 39 wt.%, respectively.

To demonstrate the internal distribution of carbon and MnO$_x$ phase in the amorphous MnO$_x$–C particles, the particles were heated in air at 310 °C for 0.5 h to remove the carbon. Since carbon was oxidized at 300 °C, a slightly higher temperature of 310 °C and a short time of 0.5 h were selected to minimize any MnO$_x$ phase growth. The TEM image of the amorphous MnO$_x$–C nanoparticle before and after the carbon removal is shown in **Figure 5**a. It is clear that after the carbon removal the uniform MnO$_x$–C particle reveals an underlying porous MnO$_x$, consisting of aggregated MnO$_x$ primary particles (~5 nm),
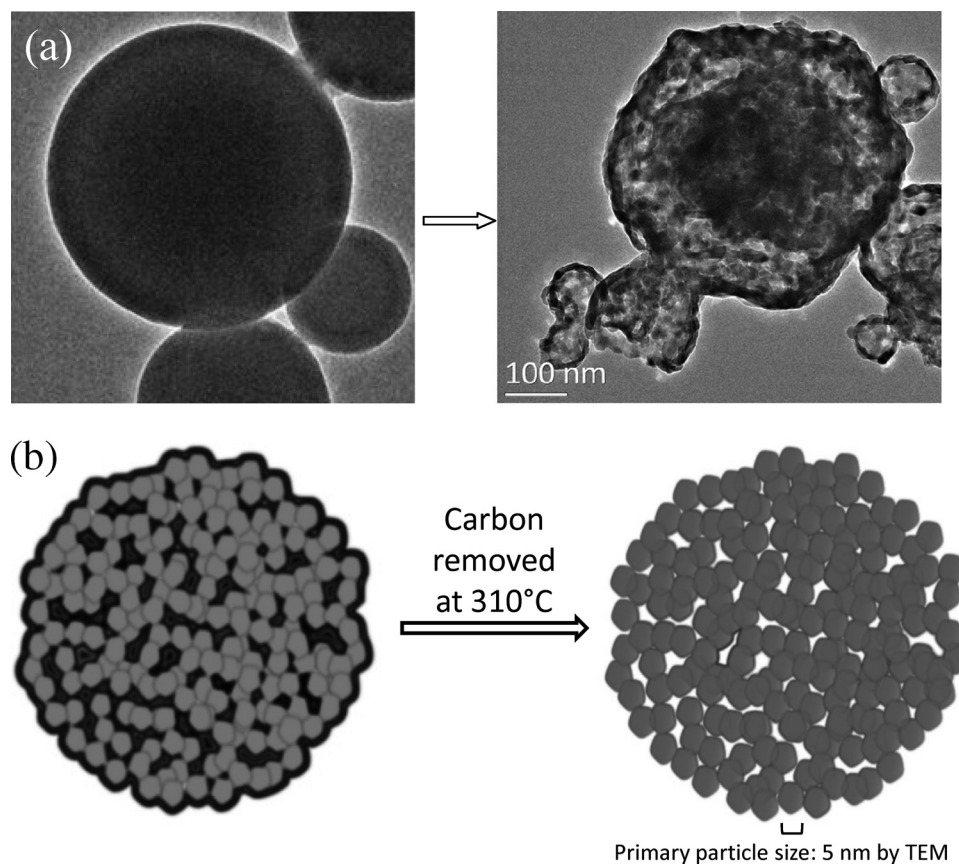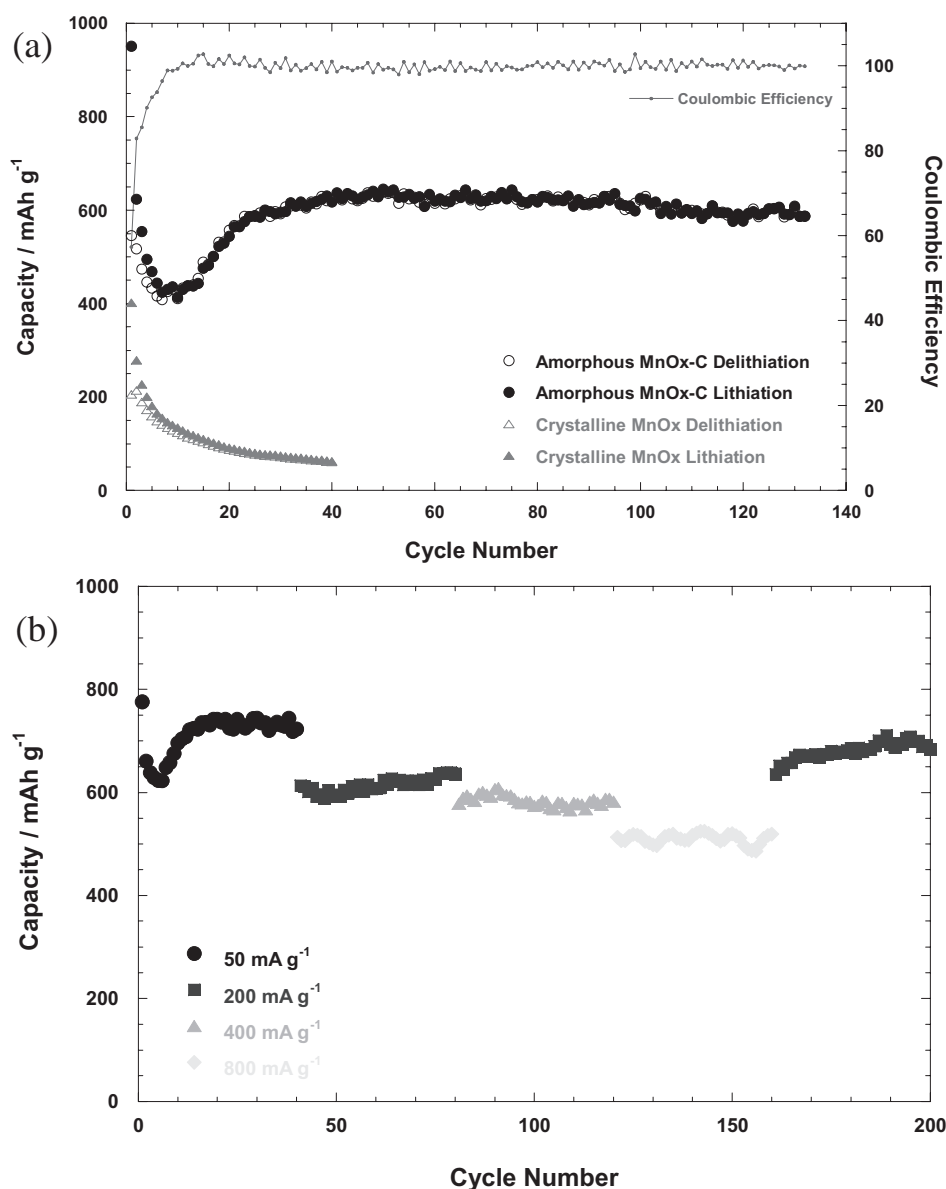
Figure 5. a) TEM image of the amorphous MnO$_x$–C nanoparticles before and after carbon removal at 310 °C, b) Schematic representation of MnO$_x$–C phase structure before and after carbon removal.

which is very similar in structure to the pure MnO$_x$ synthesized in the absence of sucrose (Figure 4). Figure 5a demonstrates that carbon is interdispersed in the MnO$_x$-C particles, as represented schematically in Figure 5b. Moreover, N$_2$ adsorption surface area measurement (Figure S3 in the Supporting Information) confirms the higher surface area and porosity of the particles after carbon removal. As the N$_2$ adsorption isotherms shown in Figure S3, the surface area after carbon removal is 1.7 times higher than before the carbon removal (40.4 m^2 g^{-1} and 24.4 m^2 g^{-1}, respectively), which also indicates the interdispersed structure of MnO$_x$–C nanoparticles.

2.2. Electrochemical Performance

Owing to the unique structure, the amorphous MnO$_x$–C nanoparticles have demonstrated superior electrochemical performance as anode materials for Li-ion batteries. As shown in **Figure 6**a, the amorphous MnO$_x$–C nanoparticles showed a high reversible capacity of approximately 650 mAh g^{-1} under 200 mA g^{-1} charge/discharge current, which is two-fold of the graphite anode capacity. It also showed exceptional capacity retention of 93% after more than 130 cycles. By contrast, the crystalline MnO$_x$ nanoparticles showed very low reversible capacity (200 mAh g^{-1}) and poor cycling stability, which is

consistent with reported results.[17,20,23] Based on the 39 wt.% MnO$_x$ (961 mAh g^{-1} theoretical capacity) content estimated previously, 375 mAh g^{-1} capacity could be attributed to MnO$_x$, and 275 mAh g^{-1} could be attributed to the carbon, consistent with the previously reported capacity of disordered carbon from pyrolysis.[10] The irreversible capacity in the first cycle was 40% that could be mainly due to the partially irreversible MnO$_x$ conversion reaction with Li, and the formation of the SEI in the first few lithiation and delithiation cycles.[12] Since the amount of SEI is reduced by the carbon, the 40% irreversible capacity of the amorphous MnO$_x$-C is actually much lower than that of nano-Mn$_2$O$_3$ (72%) and nano-Mn$_3$O$_4$ (59%) with similar particle sizes.[12] The coulombic efficiency of the amorphous MnO$_x$–C in the subsequent cycles quickly rose to 100% and remained stable during the cycling. The 100% coulombic efficiency implies the absence of new SEI formation during cycling due to carbon blocking liquid electrolyte penetration into MnO$_x$–C particles, thus reducing the contact area between MnO$_x$ and electrolytes. The capacity retention and coulombic efficiency of the amorphous MnO$_x$–C particles are the highest among the reported Mn$_3$O$_4$ and Mn$_2$O$_3$ anode materials. Due to the high diffusivity of Li in carbon (~10^{-9} cm^2 s^{-1}),[26] the Li could easily diffuse into MnO$_x$ through carbon, resulting in a high rate performance. Figure 6b shows the superior rate capability of the amorphous MnO$_x$–C nanoparticles, which could maintain 500 mAh g^{-1} of

www.MaterialsViews.com

ADVANCED
FUNCTIONAL
MATERIALS
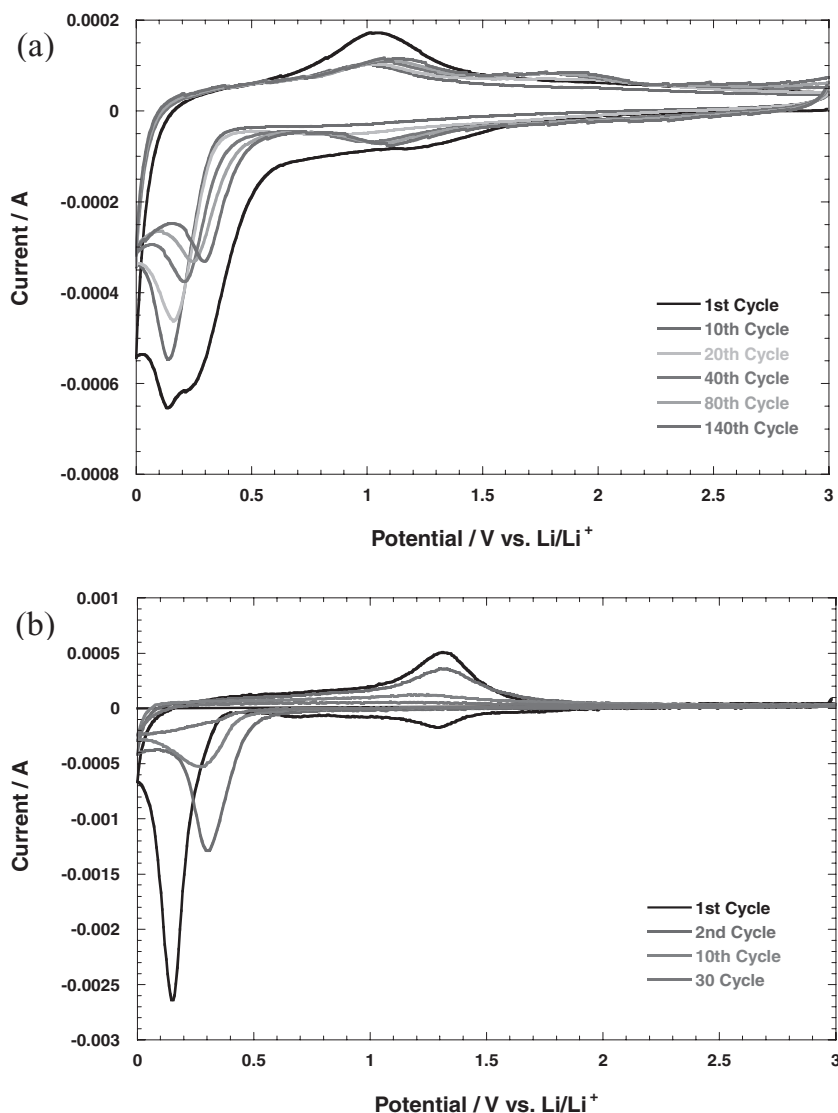www.afm-journal.de

FULL PAPER

Figure 6. a) Cyclability and b) rate capacity of the amorphous MnO_x–C nanoparticles.

capacity under 800 mA g⁻¹ charge/discharge current. Moreover, the capacity under 200 mA g⁻¹ charge/discharge rate was fully recovered when the current was reduced back to 200 mA g⁻¹ after 160 cycles.

The better capacity retention of amorphous MnO_x–C nanoparticles over the crystalline MnO_x can be partially attributed to the low volume change of amorphous MnO_x in the conversion reaction in the first lithiation compared with the crystalline MnO_x, which could enhance the structure stability of MnO_x–C. As shown in the continuous cyclic voltammetry (CV) scans in **Figure 7**, the conversion reaction of the amorphous MnO_x occurred in a broad potential range while the phase transformation of crystalline MnO_x during conversion reaction occurred in a narrower potential range, indicating lower stress/strain for

amorphous MnO_x compared with crystalline MnO_x. The low stress/strain was evidenced by the similar lithiation potential in continuous CV cycles of the amorphous MnO_x–C shown in Figure 7a. In contrast, the lithiation potential of crystalline MnO_x in the second cycle was 0.2 V higher than that in the first lithiation, as shown in Figure 7b. The increased lithiation potential of crystalline MnO_x after the first lithiation has been widely reported in the literature,[7,8,12] and is attributed to the high stress/strain caused by the large volume change of crystalline MnO_x in the conversion reaction. The CV measurements in Figure 7 also revealed the different conversion reaction processes of these two electrodes. As demonstrated in the representative curves from the continuous CV scan of amorphous MnO_x–C nanoparticles, a broad shoulder gradually

Figure 7. Representative cyclic voltammetry curves from continuous cycling of amorphous MnO_x–C nanoparticles (a) crystalline MnO_x nanoparticles (b).

amorphous MnO_x–C and 1.3 V for crystalline MnO_x particles. It is worth pointing out the pair of redox peaks for amorphous MnO_x–C at high potential which gradually appeared after approximately 20 lithiation/delithiation cycles. This redox pair, 1.1 V for lithiation and 1.8 V for delithiation, is attributed to the reaction between Mn(II) and high oxidation state Mn. It contributes to 15% to 20% of the overall capacity. It can be speculated that after a number of cycles, the conversion reaction kinetics in amorphous MnO_x–C is improved by formation of defects during the cycling, resulting in a lower overpotential. Therefore, the Mn(II) in amorphous MnO_x–C could be re-oxidized back to a higher oxidation state, indicated by the emerging redox peak pair at 1.1 V for lithiation and 1.8 V for delithiation. In the contrast, the Mn(II) in crystalline MnO_x could not be re-oxidized to a higher state as shown in Figure 7b. The irreversible conversion reaction of crystal MnO_x due to the high phase-transformation resistance of crystalline MnO_x has been reported by Chen and co-workers.[12] Therefore, it is clear that the conversion reaction of amorphous MnO_x–C is more reversible than that of crystalline MnO_x.
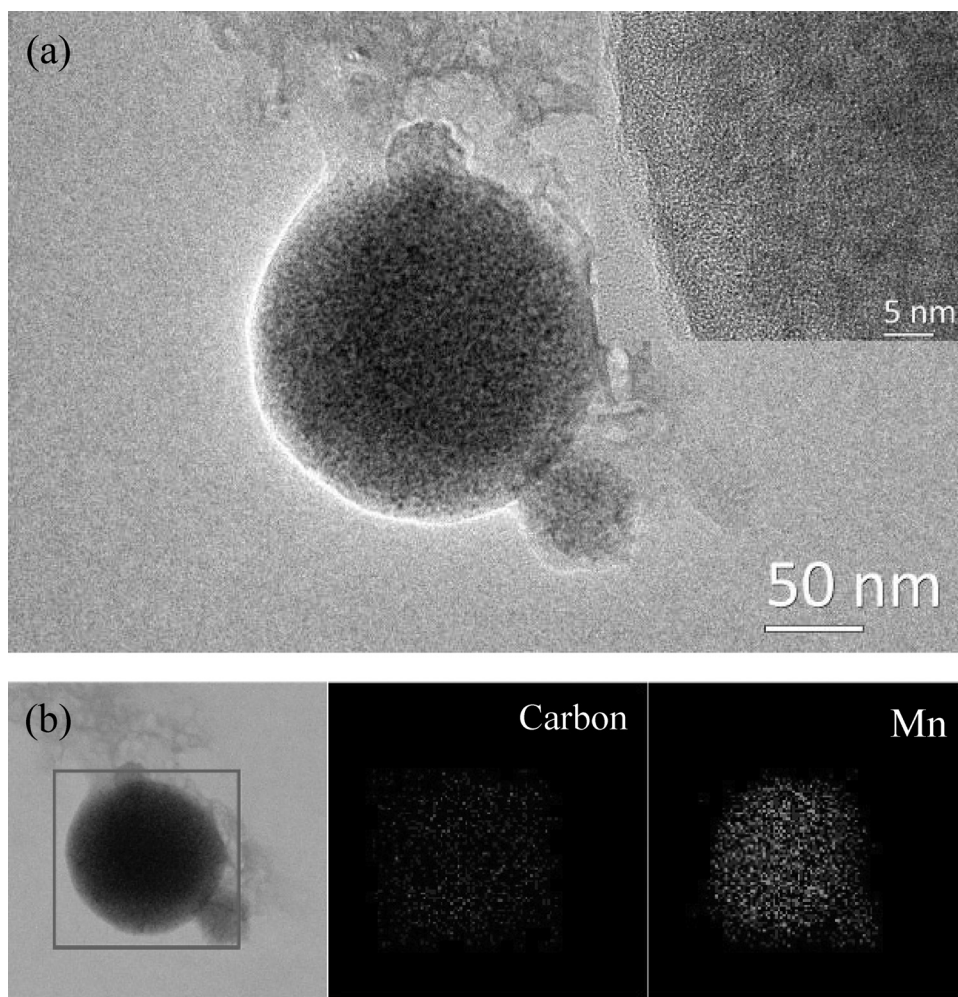
During the continuous CV cycling (Figure 7a), the shape of the two pairs of redox peaks for amorphous MnO_x–C gradually changed: the pair of redox peaks at low potential (0.2 V for reduction and 1.0 V for oxidation) became smaller and broader and an new redox pair appeared at high potential (1.1 V for reduction and 1.8 V for oxidation) with increased number of cycles and the integrated peak area went through a decreasing–increasing–stabilizing process, accompanied with the peak shape change. This evolution might associate with accumulation of defects/strain/stress energy in amorphous MnO_x–C particles. Since the integrated peak area was equal to the capacity, the continuous CV cycling behavior of the amorphous MnO_x–C nanoparticles was consistent with the decreasing–increasing–stabilizing behavior of the capacity retention curve shown in Figure 6a (the "U" shape in the plot). The mechanism behind the "U" shaped capacity retention curve is not clear, but may be attributed to mixed effects of Mn cluster aggregation inside secondary MnO_x particles and reversibility improvement of the conversion reaction in amorphous MnO_x due to formation of defects and deformation. For comparison we show the continuous CV cycling of the crystalline MnO_x nanoparticles in Figure 7b, which clearly shows an inferior performance: the redox peaks quickly diminished and no new redox pair occured, and the CV curve became flat after only 30 cycles.

Based on the different structures and electrochemical performance of these two types of manganese oxide particles, it was

appeared at 1.2 V and merged to the main reduction peak at 0.2 V in the first reduction process. The reaction current in the potential range between 0.8 V and 0.5 V was reduced in the subsequent cycles due to formation of a stable SEI in the first a few cycles. In addition, the intensity of the main reduction peak at 0.2 V was also reduced in the subsequent cycles. This broad shoulder, and the irreversible portion of the 0.2 V reduction peak could be attributed to the partially irreversible reduction of Mn ions from higher oxidation state to lower oxidation state and the formation of SEI film. As shown in the CV curve of the first cycle, the Mn(averagely +2.74) in both amorphous and crystalline MnO_x was reduced to Mn(II) at approximately 1.2 V for amorphous MnO_x–C and 1.3 V for crystalline MnO_x, and further reduced to Mn(0) at approximately 0.2 V in the first lithiation process. The Mn(0) could only be re-oxidized back to Mn(II) in the first delithiation at approximately 1.0 V for

Materials
Views

www.MaterialsViews.com

ADVANCED
FUNCTIONAL
MATERIALS
www.afm-journal.de

clear that the high capacity and superior capacity retention of the amorphous MnO_x–C nanoparticles should be attributed to its amorphous nature and unique interdispersed MnO_x-carbon structure. The conversion reaction of amorphous MnO_x is more reversible, and faster than that of conventional crystalline MnO_x materials. The uniformly interdispersed carbon in amorphous MnO_x could function as barriers to prevent the aggregation of the Mn metal grains during the repeated conversion reaction. The carbon could also function as a mixed electron and Li ion conductive environment to improve the kinetics of the conversion reaction, thus resulting in better rate performance. The high structural stability of amorphous MnO_x–C particles was confirmed by the TEM images and XRD analysis of postcycling amorphous MnO_x–C. **Figure 8**a shows the TEM image of the MnO_x–C nanoparticle after over 100 cycles. The TEM image demonstrates that the MnO_x–C nanoparticles retained the original spherical shape after intensive cycling, while the EDS mapping shown in Figure 8b demonstrates that the inter-dispersion of MnO_x and carbon is still uniform, which could be attributed to the role of carbon preventing agglomeration of MnO_x clusters. XRD (Figure S4 in the Supporting Information) showed
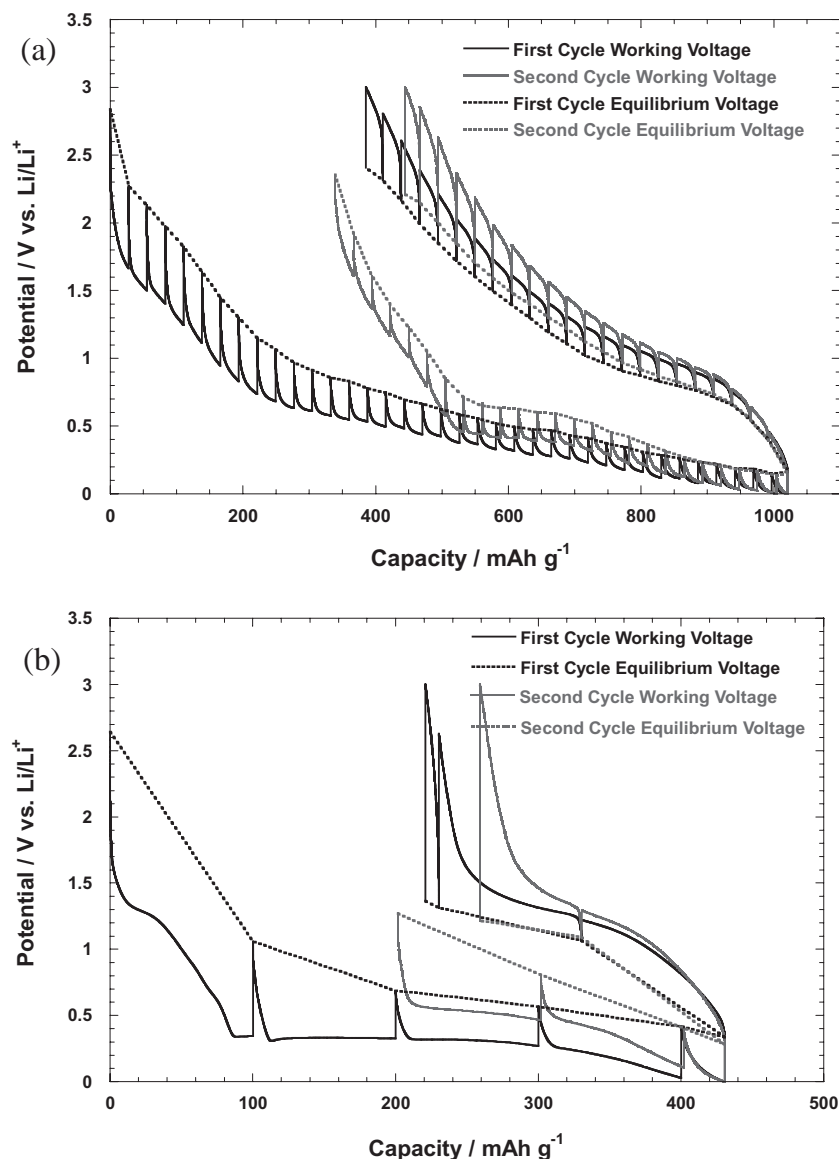
that MnO_x–C nanoparticles still retained an amorphous structure after 100 cycles.

Since the amorphous structure of MnO_x lowers the resistance for the conversion reaction, and the interdispersed carbon in MnO_x accelerates the electron/Li$^+$ conduction and charge-transfer reaction, it can be expected that the amorphous MnO_x–C nanoparticles should have faster reaction kinetics than that of crystalline MnO_x. The kinetics of the conversion reaction can be correlated to the overpotential, i.e., the difference between equilibrium charge/discharge voltage and working voltage: inferior kinetics results in higher overpotential. The overpotentials of amorphous MnO_x–C and crystalline MnO_x at different lithiation/delithiation levels were investigated using GITT as shown in **Figure 9**a and Figure 9b, respectively. In addition to kinetics, GITT can also yield thermodynamic properties such as the equilibrium potential and potential hysteresis.[27] The overpotential of the amorphous MnO_x–C in the first lithiation gradually decreased with lithiation because: 1) the defects and deformation generated from the volume change in initial lithiation decreased the resistance in subsequent lithiation processes; and 2) the electronic conductivity of the converted

Figure 8. a) TEM images and b) EDS mapping image of distribution of elemental carbon and Mn of the post-cycling amorphous MnO_x–C nanoparticles.

**ADVANCED
FUNCTIONAL
MATERIALS**

www.afm-journal.de

FULL PAPER

Materials Views

www.MaterialsViews.com

Figure 9. GITT curves of amorphous MnO$_x$–C nanoparticles (a) and crystalline MnO$_x$ nanoparticles (b).

3. Conclusion

Amorphous MnO$_x$-carbon nanoparticles were synthesized by a spray pyrolysis as the anode material for Li-ion batteries. The particles have a unique structure with uniform inter-dispersed amorphous manganese oxide and carbon, which provides high capacity and conductivity, respectively. Such a structure effectively accelerates the conversion reaction, prevents the agglomeration of the Mn metal grains during the conversion reaction with Li, thus significantly improving the cyclability. The uniform distribution of carbon improves the electrochemical reaction kinetics, which results in superior rate capacity and lowers over-potentials. The unique structure of the amorphous MnO$_x$–C nanoparticles in this study demonstrates the best anode performance for manganese oxide to date, and introduces spray-pyrolysis as a very promising technique for electrode material production.

4. Experimental Section

MnO$_x$–C nanoparticles were prepared by a spray pyrolysis method as illustrated in Figure 1. Manganese(II) nitrate hydrate (0.716g, Sigma–Aldrich) and sucrose (1.37g, Sigma–Aldrich) was dissolved in 20 mL distilled water. The solution was atomized with argon in a collision-type nebulizer, and subsequently dried with a silica gel diffusion dryer, before entering a tubular furnace at 600 °C. The nominal residence time in the heated region is ~1 s. Thermal decomposition of manganese(II) nitrate yields amorphous manganese oxide, and sucrose carbonization. The final product, amorphous MnO$_x$–C nanoparticles were collected on a 0.4 μm (pore size) DTTP Millipore filter. As comparison, pure crystalline manganese oxide nanoparticles were also synthesized through the same process with no sucrose added in the precursor solution.

Transmission electron microscopy (TEM) and energy-dispersive X-ray spectroscopy (EDS) were performed using a field-emission transmission electron microscope (JEOL JEM 2100F). X-ray diffraction (XRD) was performed on a Bruker Smart1000 using Cu Kα radiation. Thermogravimetric analysis (TGA) was carried out (TA instruments) with a heating rate of 10 °C min^{-1} in air. The porosity surface area of the MnO$_x$–C nanoparticles was analyzed by nitrogen adsorption measurement (TriStar II 3020). X-ray photoelectron spectroscopy (XPS) was conducted with a high-sensitivity Kratos AXIS 165 spectrometer to analyze the oxidation state of the manganese oxide.

The electrode was prepared by mixing the MnO$_x$–C nanoparticles (80 wt.%) with carbon black (10 wt.%) and polyvinylidene fluoride (10 wt.%) in n-methyl-2-pyrrolidone. The obtained ink was coated on a nickel foil (99.5%, Alfa Aesar) current collector, followed by drying in a vacuum oven at 110 °C for 24 h. Two-electrode coin cells with lithium foil as the counter electrode were assembled in argon-filled glove box. Electrolyte (Novolyte Technologies) consisting of 1 M LiPF$_6$ in a mixture of ethylene carbonate/diethyl carbonate (1:1 by volume) was used with a micro-porous polymer membrane separator (Celgard 3501). The cells were charged and discharged between 0 V and 3 V (versus Li/Li$^+$)

phase (Li$_2$O + Mn) is higher than MnO$_x$. The defects and deformation energy introduced by the first lithiation also decreased the overpotential of amorphous MnO$_x$–C in the second lithiation. A significant result from Figure 9a is that the overpotential for both lithiation and delithiation was only approximately 0.2 V (difference between the working voltage and equilibrium voltage), and the previously reported lowest overpotential for manganese oxide was between 0.4 V and 0.5 V.[7] The low overpotential resulted in low charge/discharge hysteresis. In contrast, crystalline MnO$_x$ showed a 2× higher overpotential than that of the amorphous MnO$_x$–C nanocomposite, although the former had high contact area between MnO$_x$ and electrolyte, and the particle size of the two materials is nearly the same. Therefore, the amorphous nature of the MnO$_x$ and the inter-dispersed carbon structure greatly accelerated the conversion reaction.

www.MaterialsViews.com

ADVANCED
FUNCTIONAL
MATERIALS
www.afm-journal.de

FULL PAPER

using an Arbin battery test station. Galvanostatic intermittent titration technique (GITT) were performed by charging/discharging the cell using a current of 100 mA g^{-1} for 1 h, and a rest for 16 h until the cut-off voltage limits were reached. Prior to post-cycling characterization of the MnO_x–C nanoparticles, the cell was charged at 3 V for 48 h to ensure full extraction of Li. Cyclic voltammetry (CV) measurements were carried out with a scan rate of 0.1 mV s^{-1} on Solartron 1287/1260 analyzer or Gamry Reference 3000 Potentiostat/Galvanostat/ZRA.

Supporting Information

Supporting Information is available from the Wiley Online Library or from the author.

Acknowledgements

[1] H. Li, Z. Wang, L. Chen, X. Huang, *Adv. Mater.* **2009**, *21*, 4593.
[2] P. Poizot, S. Laruelle, S. Grugeon, L. Dupont, J.-M. Tarascon, *Nature* **2000**, *407*, 496.
[3] H. Li, P. Balaya, J. Maier, *J. Electrochem. Soc.* **2004**, *151*, A1878.
[4] H. Li, G. Richter, J. Maier, *Adv. Mater.* **2003**, *15*, 736.
[5] A. Debart, L. Dupont, P. Poizot, J. B. Leriche, J.-M. Tarascon, *J. Electrochem. Soc.* **2001**, *148*, A1266.
[6] P. Balaya, H. Li, L. Kienle, J. Maier, *Adv. Funct. Mater.* **2003**, *13*, 621.
[7] X. Yu, Y. He, J. Sun, K. Tang, H. Li, L. Chen, X. Huang, *Electrochem. Commun.* **2009**, *11*, 791.
[8] K. Zhong, X. Xia, B. Zhang, H. Li, Z. Wang, L. Chen, *J. Power Sources* **2010**, *195*, 3300.
[9] J. Liu, Q. Pan, *Electrochem. Solid-State Lett.* **2010**, *13*, A139.
[10] B. Sun, Z. Chen, H.-S. Kim, H. Ahn, G. Wang, *J. Power Sources* **2011**, *196*, 3346.
[11] S. Nayak, S. Malik, S. Indris, J. Reedijk, A. K. Powell, *Chem. Eur. J.* **2010**, *16*, 1158.
[12] X. Fang, X. Lu, X. Guo, Y. Guo, Y. Mao, Y. Hu, J. Wang, Z. Wang, F. Wu, H. Liu, L. Chen, *Electrochem. Commun.* **2010**, *12*, 1520.
[13] M. Toupin, T. Brousse, D. Belanger, *Chem. Mater.* **2002**, *14*, 3946.
[14] M. Wu, P. Chiang, J. Lee, J. Lin, *J. Phys. Chem. B* **2005**, *109*, 23279.
[15] M. Wu, P. Chiang, *Electrochem. Commun.* **2006**, *8*, 383.
[16] B. Li, G. Rong, Y. Xie, L. Huang, C. Feng, *Inorg. Chem.* **2006**, *45*, 6404.
[17] H. Xia, M. Lai, L. Lu, *J. Mater. Chem.* **2010**, *20*, 6896.
[18] D. Pasero, N. Reeves, A. R. West, *J. Power Sources* **2005**, *141*, 156.
[19] Q. Fan, M. S. Whittingham, *Electrochem. Solid-State Lett.* **2007**, *10*, A48.
[20] H. Wang, L. Cui, Y. Yang, H. S. Casalongue, J. T. Robinson, Y. Liang, Y. Cui, H. Dai, *J. Am. Chem. Soc.* **2010**, *132*, 13978.
[21] J. Fan, T. Wang, C. Yu, B. Tu, Z. Jiang, D. Zhao, *Adv. Mater.* **2004**, *16*, 1432.
[22] F. Cheng, Z. Tao, J. Liang, J. Chen, *Chem. Mater.* **2008**, *20*, 667.
[23] A. L. M. Reddy, M. M. Shaijumon, S. R. Gowta, P. M. Ajayan, *Nano Lett.* **2009**, *9*, 1002.
[24] L. Ji, X. Zhang, *Electrochem. Commun.* **2009**, *11*, 795.
[25] O. Delmer, P. Balaya, L. Kienle, J. Maier, *Adv. Mater.* **2008**, *20*, 501.
[26] H. Guo, X. Li, X. Zhang, H. Wang, Z. Wang, W. Peng, *New Carbon Mater.* **2007**, *22*, 7.
[27] Y. Zhu, C. Wang, *J. Power Sources* **2011**, *196*, 1442.